Effect of Large-Angle Scattering on Particle Transport and Heat Flux in Advanced Divertor Magnetic Field Configurations

Daisuke UMEZAKI, Hideaki MATSUURA and Kazuo HOSHINO[1)]

Department of Applied Quantum Physics and Nuclear Engineering, Kyushu University, Motooka, Fukuoka 819-0395, Japan
[1)]*Faculty of Science and Technology, Keio University, Yokohama, Kanagawa 223-8522, Japan*

(Received 6 September 2023 / Accepted 26 November 2023)

Divertor heat loads are one of the most significant issues affecting fusion reactors. Atomic processes play a crucial role in reduction of the divertor heat load. Notably, elastic scattering between ions and neutral particles can be characterized as large-angle scattering. A large fraction of ion energy is transferred to neutral particles, and the ion direction can be significantly changed by a single large-angle scattering event. In abundant neutral particle regions such as divertor plasmas, the large-angle elastic scattering results in additional ion transport perpendicular to magnetic field lines. Effect of the additional ion transport is expected to be significant at low magnetic field strength and long Larmor radii, such as in a case of advanced divertors (e.g., Super-X and Snowflake divertors). In this study, we investigated the effect of the large-angle elastic scattering at low magnetic field strength and long divertor legs with reference to advanced divertor configurations using an orbital calculation. The large-angle elastic scattering transport is seen to cause a spread in density profiles and a reduction of heat flux. The results of this study show that for the short (long) leg divertor configuration like JT-60U (advanced divertor), the peak heat flux is reduced by around 15% (21%) when the magnetic field strength is 0.5 T in comparison to the model that assumes no guiding center movement due to the elastic scattering. It is also shown that the assumption of isotropic elastic scattering with neutral particles leads to excessive suppression of ion flows.

Keywords: elastic scattering, large-angle scattering, divertor, edge plasma, atomic process, advanced divertor

DOI: 10.1585/pfr.19.1403003

1. Introduction

Reduction of heat loads on divertor plates is one of the most important issues to be addressed. A (partial) detached divertor will be employed to reduce the divertor heat load in various fusion devices, such as ITER, JT-60SA and the Japan's DEMO reactor. Interaction between plasma and neutral particles and power radiation resulting from impurity injection play a significant role in establishing the detached divertor. The interactions with neutral particles such as charge exchange and elastic scattering, facilitate diffusion of ions. The power radiation reduces electron temperature and facilitates volume recombination. In the Japan's DEMO reactor, 80% of the inflow power from the core plasma to the edge plasma regions to suppress the heat load peak of less than 10 MW/m^2 [1–3]. Since exhaust power of future fusion devices is expected to be larger, it is important to propose different heat load reduction methods.

Advanced divertors, such as the Super-X divertor [4,5] and the Snowflake divertor [6,7], have been proposed to reduce the divertor heat load. To configure advanced divertors, the designs have to be modified, and additional coil currents are necessary. In the advanced divertor methods, two factors are modified: 1) the divertor legs are lengthened to increase the radiated power and facilitate interactions with neutral particles, and 2) the magnetic flux is expanded to induce particle diffusion. Effectiveness of the advanced divertors has been evaluated using the SOLPS software package [8–10]. Design of advanced divertors for the previous Japanese DEMO reactor has also been evaluated [11–13] using the SONIC software package [14, 15]. Most of integrated codes solve the fluid momentum balance only in a direction parallel to magnetic field lines, thus the atomic processes are taken into account in a source term of the parallel momentum balance. For a direction perpendicular to magnetic field lines, most of integrated codes, including the SONIC code, solve a diffusion equation and do not consider atomic processes such as the elastic scattering. In the SOLPS code, atomic processes are considered in a direction perpendicular to magnetic field lines. However, the effect of the elastic scattering on ion transport perpendicular to magnetic field lines is not fully clear. Atomic processes, including the elastic scattering, are basic cause of particle transport.

From a quantum point of view, it is impossible to distinguish elastic scattering from charge exchange between identical nuclei, such as deuterons and deuterium atoms [16]. In this study, the collision process between a deuteron ion and a deuterium atom is simply referred to as "the elastic scattering". In order to adequately assess effect of the

author's e-mail: umezaki.daisuke.786@s.kyushu-u.ac.jp

elastic scattering, following unique characteristics should be considered. 1) The elastic scattering can be characterized as large-angle scattering in contrast to Coulomb scattering. Figure 1 (a) shows the differential cross sections of the elastic scattering between deuteron and deuterium at some center-of-mass collision energy E_{CM} [16] in black, red, and blue lines. The cross sections are also shown in black, red, and blue dashed lines when the elastic scattering is assumed to be isotropic scattering. The Coulomb scattering cross section between deuteron and triton is drawn in a green line. As described later, kinetic simulation models often assume the elastic scattering to be isotropic. In order to compare the results of the actual anisotropic elastic scattering with those of the isotropic assumption, a case of isotropic assumption is also simulated in this study. Figure 1 (b) shows the scattering of a particle colliding with a stationary target particle. The differential cross section $2\pi \sin\theta(d\sigma/d\Omega)$ shown in Fig. 1 (a) means the probability of the particle being scattered within the circle $2\pi \sin\theta d\theta$ in Fig. 1 (b). A change in velocity after scattering is small for small-angle scattering, while a change in velocity is large for large-angle scattering. The probability of the large-angle elastic scattering is several orders of magnitude higher than in the case of isotropic scattering. In the actual elastic scattering between deuterons and deuterium atoms, large- and small-angle scattering occur at almost the same level, in contrast to Coulomb scattering. 2) In large-angle scattering, a large fraction of the ion/neutral energy is transferred from the neutrals/ions, and the particle flight direction can be significantly shifted during a single scattering event. Our previous study [17,18] showed that ions are transported in the radial direction by the large-angle elastic scattering. In Ref. [18], an orbital calculation model that can treat ion transport due to the large-angle elastic scattering has been developed.

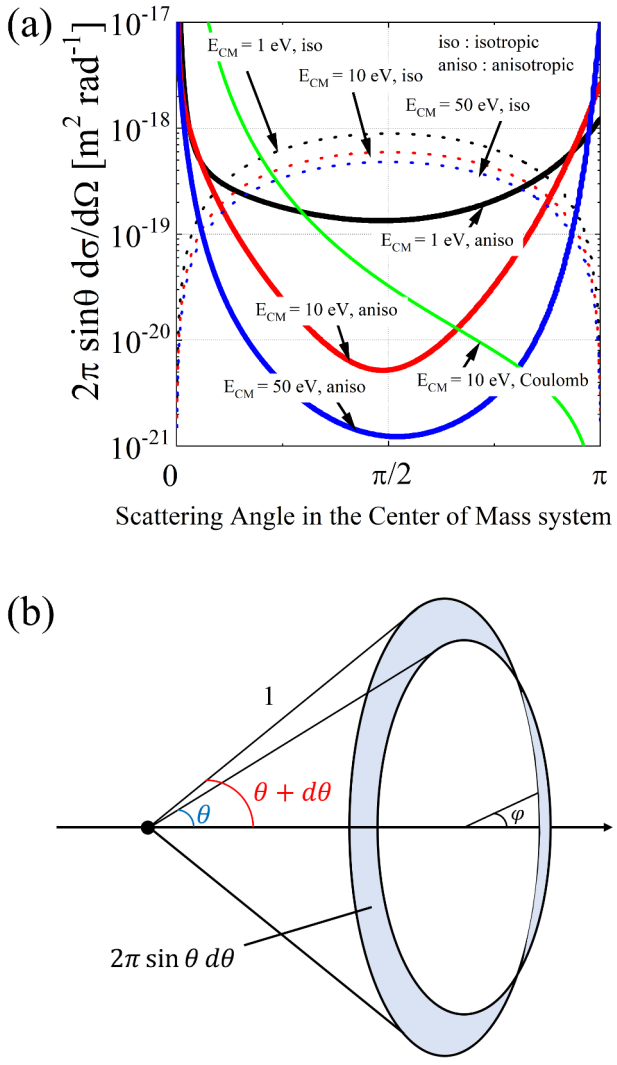

Fig. 1 (a) Differential and isotropic (Coulomb) cross section $2\pi \sin\theta d\sigma/d\Omega$ of the elastic scattering between deuteron and deuterium (triton) [16], and (b) a schematic view of a particle colliding with a stationary target particle.

Particle-in-cell models can adequately treat the ion's kinetics. A lot of PIC codes have been developed (e.g., BIT1 code [19–21] and PARASOL code [22–24]) to simulate edge plasmas. These codes have produced significant results in the study of a magnetized plasma-wall-transition layer and effect of various drifts. The BIT1 code simulates plasmas in one spatial and three velocity dimensions. The PARASOL code traces ions in 2D space with considering $\vec{E} \times \vec{B}$ drift. The 1D space model cannot account for particle transport perpendicular to magnetic field lines. Moreover, if the elastic scattering between ions and neutrals is treated as isotropic, the effect of large-angle scattering may not be adequately assessed.

Particle transport is generated by motion of a guiding center to another magnetic field line via various scattering events. The distance covered by a guiding center in a radial direction is longer in large-angle scattering than in small-angle scattering, and the distance is inversely proportional to magnetic field strength. In tokamak devices, the magnetic field consists of toroidal (B_T) and poloidal (B_P) magnetic fields and its strength mainly depends on the toroidal magnetic field. In the Super-X divertor, divertor plates are placed farther than in a standard divertor position. Since the toroidal field is proportional to $1/R$, the toroidal field is expected to be weakened in the Super-X divertor configuration. In such small magnetic fields, the large-angle elastic scattering effect on particle transport can be enhanced.

In this study, we investigate the effect of large-angle elastic scattering on particle transport in configurations similar to that of the JT-60U divertor (short leg) and advanced divertors (long leg) by simulating fuel ions using an orbit calculation [18, 25–27]. As a parameter, the toroidal magnetic field strength is changed. Background plasma values for the orbit calculation are simulated using a fluid model [28]. The large-angle elastic scattering process is properly treated with a probability function by considering the differential cross section [29–35]. Results of the

orbit calculation are discussed to evaluate the effect of the large-angle elastic scattering on ion transport and heat flux at the divertor plate. This study's results show that, at a magnetic field strength of 0.5 T, the peak heat flux in the short (long) leg divertor configuration is reduced by approximately 15% (21%) compared to a model that ignores the impact of the elastic scattering on guiding center movement. It is also shown that assuming the elastic scattering as isotropic leads to excessive suppression of ion flows.

2. Analysis Model

2.1 Mesh structure

Figure 2 shows two-dimensional (2D) schemes ($300 \times 20\,\mathrm{cm}^2$, $500 \times 20\,\mathrm{cm}^2$) that are simplified of tokamak divertor regions as a short leg and a long leg. As depicted in Fig. 2, the x-axis is aligned parallel to magnetic fields $\vec{B}$ while the y-axis is arranged perpendicular to the x-axis and parallel to the divertor plates. A uniform magnetic field from the upwind boundary to the divertor plate is assumed. The B_P is fixed to 0.2 T and the B_T is varied between 0.5 and 10.0 T. Although no fusion reactor currently generates such a high magnetic field $B_T = 10$ T, the high magnetic field simulation is performed to verify that movement of a guiding center due to the elastic scattering is reduced. In an actual fusion reactor, connection length is related to the ratio of B_T and B_P. In this research, the connection lengths (the long side of the 2D scheme) are 300 and 500 cm, regardless of the ratio. Furthermore, the upwind boundary condition is common for all calculation cases. The fluid calculation flow is the same as in Ref. [17]; however, in this study, the effect of the elastic scattering on the ion transport perpendicular to the magnetic field is not taken into account in the fluid calculation. The stationary solution of the fluid calculation is assumed to be the background plasma for the orbital calculation as described in Sec. 2.3 and the effect of the elastic scattering on ion transport is considered in the orbital simulation.

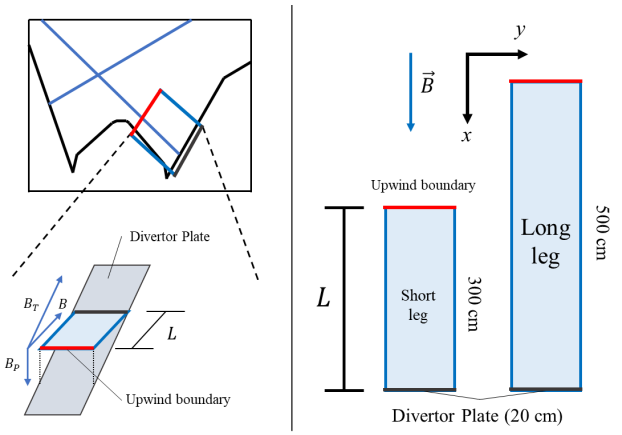

Fig. 2 Calculation scheme with reference to the divertor plasma region of the short leg divertor and long leg divertor.

2.2 Fluid and neutral models

The Braginskii equations [28] are simulated in the same way as in Ref. [17] to define the background plasma for the orbit calculation. The fluid simulation is also performed in the 2D scheme (Fig. 2). In the fluid simulation, velocity perpendicular to the magnetic field is calculated from a diffusion equation. An anomalous diffusion coefficient of $0.3\,\mathrm{m}^2/\mathrm{s}$ is used. Upwind boundary conditions are provided for the fluid simulation based on the SONIC package and the experimental values obtained for the fluid equations [36]. Boundary conditions of ion and electron heat flux at the divertor plate are set to $q_i = 3.5\, n_i v_f T_i$ and $q_e = 4.0\, n_e v_f T_e$ [37]. A flux limit parameter is implemented using the same procedure as in Ref. [38]. Deuterons and electrons are considered as plasma particles, and deuterium atoms are considered as neutral particles. The neutral particles are simulated by a simple fluid model in the same way as in Ref. [37] using a reflection coefficient R_N [39]. In the simplified neutral fluid model, ions are assumed to be neutralized and reflected at the divertor plate by considering the pitch angle between the magnetic field lines and the divertor plate. The neutral particle density profile is calculated using the method described in Ref. [37] and the total amount of neutral particles is adjusted considering the volume recombination. Figures 3 (a) and (b) show the stationary solution of the fluid calculation as the background plasma for the orbital simulation. In the fluid simulation, since the diffusion equation is applied for the transport perpendicular to the magnetic field line, the elastic scattering is considered only in a direction parallel to the magnetic field. Figure 3 illustrates the ion density n_i, neutral density n_n, ion and electron temperature T_i and T_e, and flow velocity v_f from the upwind boundary to the divertor plate on a strike point. For a typical JT-60U magnetic field $B_T = 3.0$ T and $B_P = 0.2$ T, the integrated ion flux at the divertor plate calculated via the fluid code is $5.5 \times 10^{22}\,\mathrm{s}^{-1}$ and it is within the range of reported experimental values [40].

2.3 Orbit calculation: large-angle scattering transport (LST) model

The stationary solution of the fluid equation is considered as the background plasma, and the orbit calculation for the deuterons is performed using the following method. The SONIC code [14] consists of the IMPMC code [25] and the other two codes (SOLDOR [41] and NEUT2D [41]). The IMPMC code simulates the density and temperature of the impurity ions, such as C and Ar, by Monte Carlo orbital calculations. Effect of Coulomb scattering on ion velocity is treated in the same way as in Ref. [18, 25–27]. The orbital ions experience frictional force due to the flow velocity of the background plasma. This frictional force is expressed by the following Eq. (1) and can be taken into account in the same way of the IMPMC code. An orbit of ion is calculated by solving the following

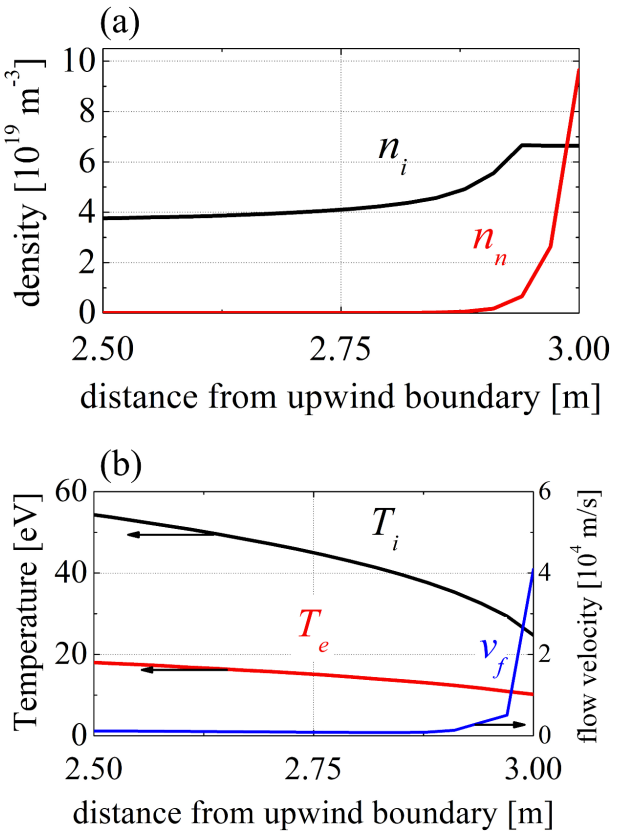

Fig. 3 The stationary solutions of (a) ion density n_i, neutral density n_n, (b) ion and electron temperature T_i and T_e, and flow velocity v_f from the upwind boundary to the divertor plate on the strike point.

equation of motion:

$$m_i \frac{dv_\parallel}{dt} = \frac{m_i(v_f - v_\parallel)}{\tau_a}, \quad (1)$$

$$\Delta y = \sqrt{2D_\perp \Delta t} \times r_G, \quad (2)$$

where m_i is the ion mass, $v_\parallel$ is the velocity of the particle parallel to the magnetic field line, v_f is the velocity of the background parallel flow, τ_a is the collision time, and Δt is the time step interval. Thermal force generated by temperature gradients is ignored. The position x of the ion guiding center after Δt is calculated from the velocity before and after Coulomb scattering. In Eq. (2), Δy is the distance travelled in a perpendicular direction to the magnetic field line, $D_\perp$ is a diffusion coefficient, and r_G is a normal random number. Similar to other integrated codes, the anomalous diffusion coefficient $D_\perp^{an} = 0.3\,\mathrm{m^2 s^{-1}}$ is used. The guiding center is traced in the 2D space and movement of the guiding center in the z-axis is ignored. In the orbit simulation, the parallel velocity $v_\parallel$, the rotation velocity $v_\perp$ and the position of the guiding center (x, y) in the 2D space are simulated. $v_\perp$ is used to obtain the kinetic energy of the orbital ion.

The steady-state plasma density $n_i^{orbital}$ and temperature $T_i^{orbital}$ are obtained using the track-length estimator method as a scoring technique [42]. Inflow particles from the upwind boundary and ionization are considered as particle sources. In total, more than 1.4×10^6 orbital particles are calculated. In this study, the elastic scattering and the recombination process are considered as atomic processes. The occurrences of the atomic processes are treated in the same way as in the IMPMC code. At each time step, the occurrence of an atomic process is determined before calculating the position of the particle after Δt. Unlike the PIC codes, electric fields are not considered, and the orbit calculation is performed only once under the fixed background plasma. Other drift velocity such as $\vec{E} \times \vec{B}$ drift is not considered to assess the pure effect of the elastic scattering on the ion transport.

The orbit calculation is continued until recombination process occurs or the particle reaches an end of the calculation area. The number of orbital particles counted in a control volume near the strike point was approximately 10^6 - 10^7. Given these values, the relative error was found to be less than 0.1%.

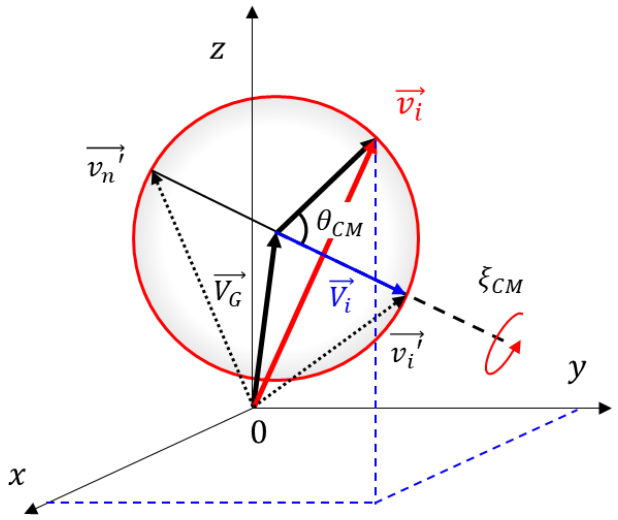

Fig. 4 Schematic of the change in the ion velocity before and after large-angle scattering.

* LST model [18, 29–35]

In this model, the velocity after the elastic scattering is calculated as same way in Ref. [18]. Figure 4 shows the relationship of the velocity between before and after the elastic scattering. $\vec{v_i}$ is the ion velocity after the elastic scattering, $\vec{V_G}$ represents the velocity of the center of mass, θ_{CM} stands for the scattering angle of the center of mass, $\vec{V}_i$ signifies the ion velocity before the scattering in the center of mass system ($\vec{V_i} = \vec{v_i'} - \vec{V_G}$), $\vec{v_i'}$ and $\vec{v_n'}$ are the ion and neutral particle velocity before the elastic scattering, and ξ_{CM} represents the angle around the axis along with $\vec{V}_i$. The velocity $\vec{v}_i$ lies on a sphere of radius $|\vec{V_i}|$ centered on $\vec{V_G}$.

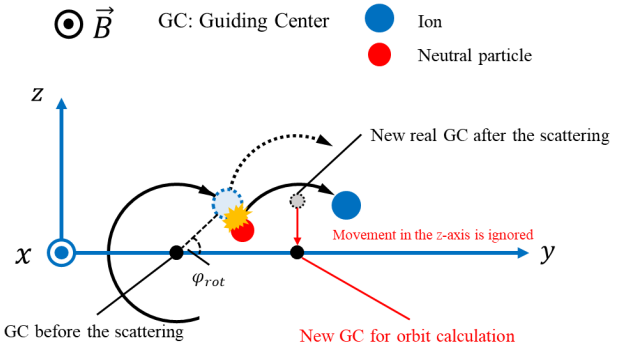

Fig. 5 Schematic of the orbital calculation.

The differential cross section is considered using the Neumann's rejection method. Figure 5 shows a schematic view of the elastic scattering in the orbit calculation. In this study, as the movement in the z-axis direction is ignored and the position of the guiding center is traced in the 2D space. The z-axis position of the guiding center before the elastic scattering is assumed to be 0. When the elastic scattering occurs, the ion position before the scattering is calculated as $(x', y' + r'_L \cos\varphi_{rot}, r'_L \sin\varphi_{rot})$ by using a rotation angle $\varphi_{rot} = 2\pi \times r_U$ on a rotational orbit. r_U is a uniform random number. The new position of the guiding center (x, y, z) after the scattering can be obtained from the new velocity $\vec{v_i}$ as follows:

$$\begin{pmatrix} x \\ y \\ z \end{pmatrix} = \begin{pmatrix} x' + r_L \times F_x/|\vec{F}| \\ y' + r'_L \cos\varphi_{rot} + r_L \times F_y/|\vec{F}| \\ r'_L \sin\varphi_{rot} + r_L \times F_z/|\vec{F}| \end{pmatrix}, \quad (3)$$

where $r_L = m|\vec{v_i}|/qB(r'_L)$ is a Larmor radius after (before) the elastic scattering, $\vec{F} = (F_x, F_y, F_z) = q\vec{v_i} \times \vec{B}$ is Lorentz force. The orbit calculation is continued using the new guiding center position (x, y).

* Models for comparison

For comparison with the LST model, we simulate three other models. 1) The Isotropic model treats the elastic scattering between ions and neutrals as isotropic scattering. 2) The second model also assumes the elastic scattering as isotropic but ignores guiding center movement via the elastic scattering (Ignoring the Guiding Center Movement model: IGM model). The typical treatment of the elastic scattering in the PIC codes [19–24] assumes it to be isotropic and, in some cases, effect of the elastic scattering on ion transport in space is not considered. 3) The anisotropic-IGM model considers the differential cross section of the elastic scattering and ignores guiding center movement. This model is required to adequately evaluate the effect of LST on the density profile at the divertor plate. Details are discussed in Sec. 3.2. In the Isotropic and IGM models, the scattering angle is calculated as $\theta_{CM} = \cos^{-1}(1 - 2 \times r_U)$ [20] to simulate the isotropic scattering. In the IGM model, the velocity after scattering is updated $\vec{v_i}$; however, the guiding center position remains unchanged. Similarly, in the anisotropic-IGM model, while the differential cross section is taken into account, the guiding center position is not updated.

Table 1 Characteristics of each orbital calculation model.

	elastic scattering	guiding center movement	similar code
LST model	anisotropic	considered	-
Isotropic model	isotropic	considered	PIC codes
IGM model	isotropic	ignored	
anisotropic-IGM	anisotropic	ignored	integrated codes

The effect of the large-angle scattering on ion transport can be evaluated by comparing the LST model with the above three models. The characteristics of each orbital calculation model are listed in Table 1. For example, by comparing the results of the LST model with those of the Isotropic model, an assessment of the effect of the anisotropic elastic scattering on ion transport can be expected. The validity of the isotropic scattering assumption could also be discussed. By comparing the LST with the anisotropic-IGM model, the impact of introducing the elastic scattering transport into an integrated code that does not consider elastic scattering for transport perpendicular to magnetic field lines could be predicted.

The reduction ratio of heat flux, which is discussed in Sec. 3.3, is expressed as follows:

$$(\text{reduction ratio}) = -\frac{(h_{LST} - h_{IGM})}{h_{IGM}} \times 100, \quad (4)$$

$$h = \frac{3}{2} n_i^{orbital} T_i^{orbital} u_i, \quad (5)$$

where u_i is the velocity of the ions and is expressed as $u_i = \sqrt{2T_i^{orbital}/m_i}$ at the divertor plate.

3. Results and Discussion

3.1 Effect of large-angle scattering on the 2D density profile

In this section, the effect of the large-angle elastic scattering on the density profile is assessed by comparing the 2D density profiles calculated by the LST model with those of the IGM model. Figure 6 displays the 2D density profiles up to 50 cm from the divertor plates for the (a) short leg divertor and (b) long leg divertor configurations at $B_T = 0.5$ T calculated via the LST and IGM models. The vertical axis is along the magnetic field. Figures 6 (a-1) and (b-1) show the result of the LST model, whilst Figs. 6 (a-2) and (b-2) show the result of the IGM model. The comparison between Figs. 6 (a-1) and (a-2) shows that LST spreads the 2D density profile perpendicular to the magnetic field lines and reduces the density peak at the low magnetic field strength. The 2D density profile is spread perpendicular to

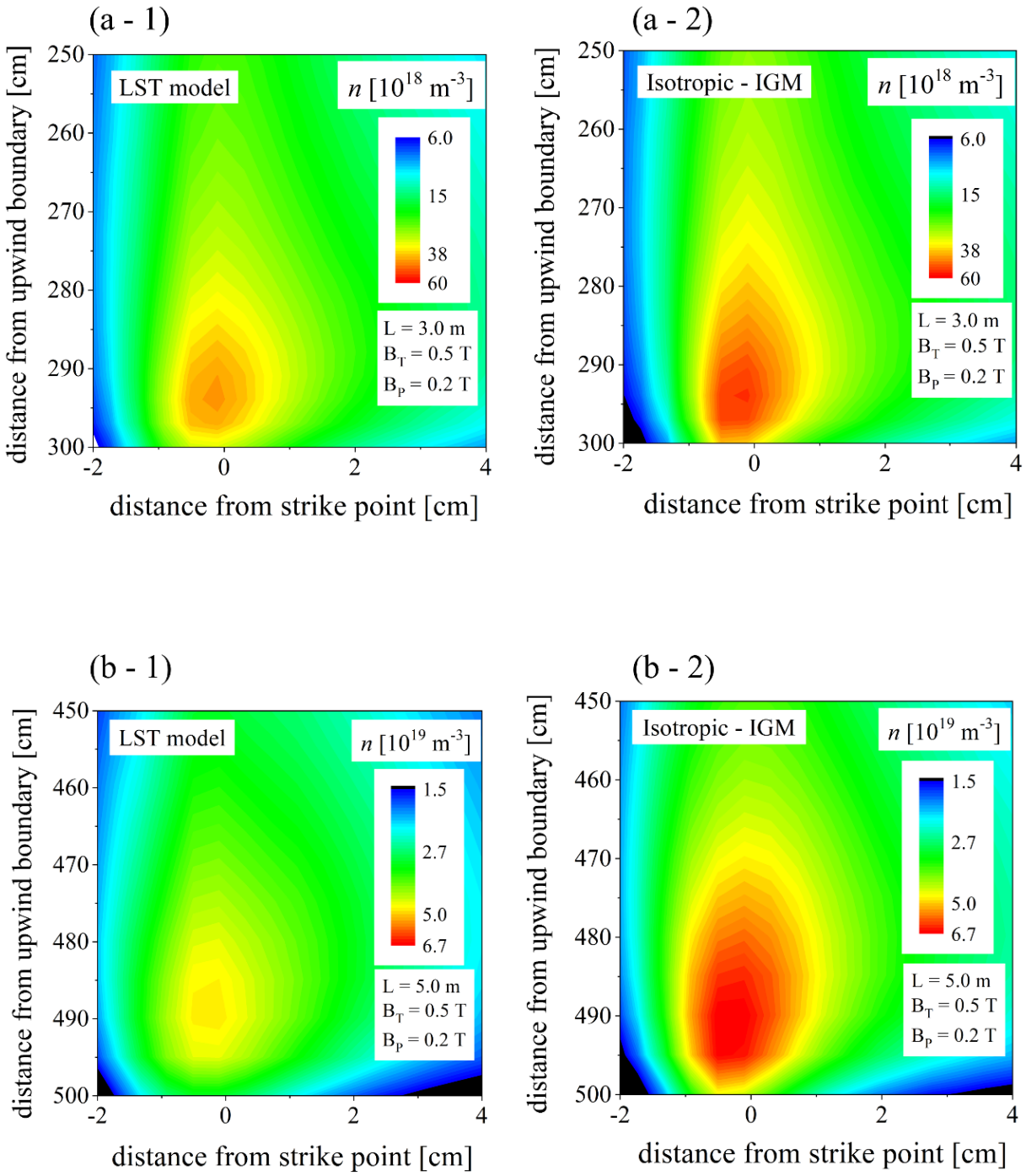

Fig. 6 2D density profiles up to 50 cm from the divertor plate in the (a) short leg divertor and (b) long leg divertor configurations calculated using the LST and IGM models.

the magnetic field lines, and the density peak is reduced as a consequence of the LST. Distance covered by ions in a single large-angle elastic scattering event is much longer than that in small-angle Coulomb scattering. It caused the additional radial ion transport and made the density profile spread. In the 2D configuration of the short leg divertor, the peak density calculated via the IGM model is around 5.30×10^{19} m^{-3}. The peak density calculated via the LST model decreases to 4.27×10^{19} m^{-3} by the large-angle elastic scattering.

In the 2D configuration of the long leg divertor, the peak density calculated via the IGM model is approximately 6.71×10^{19} m^{-3}. The peak density obtained using the LST model decreases to 4.79×10^{19} m^{-3}. Furthermore, the peak density calculated via the IGM model in strong magnetic fields ($B_T > 5.0$ T) was also higher than the that of the LST model. The same but small impact can be seen in the high magnetic strength case, as discussed in Secs. 3.2

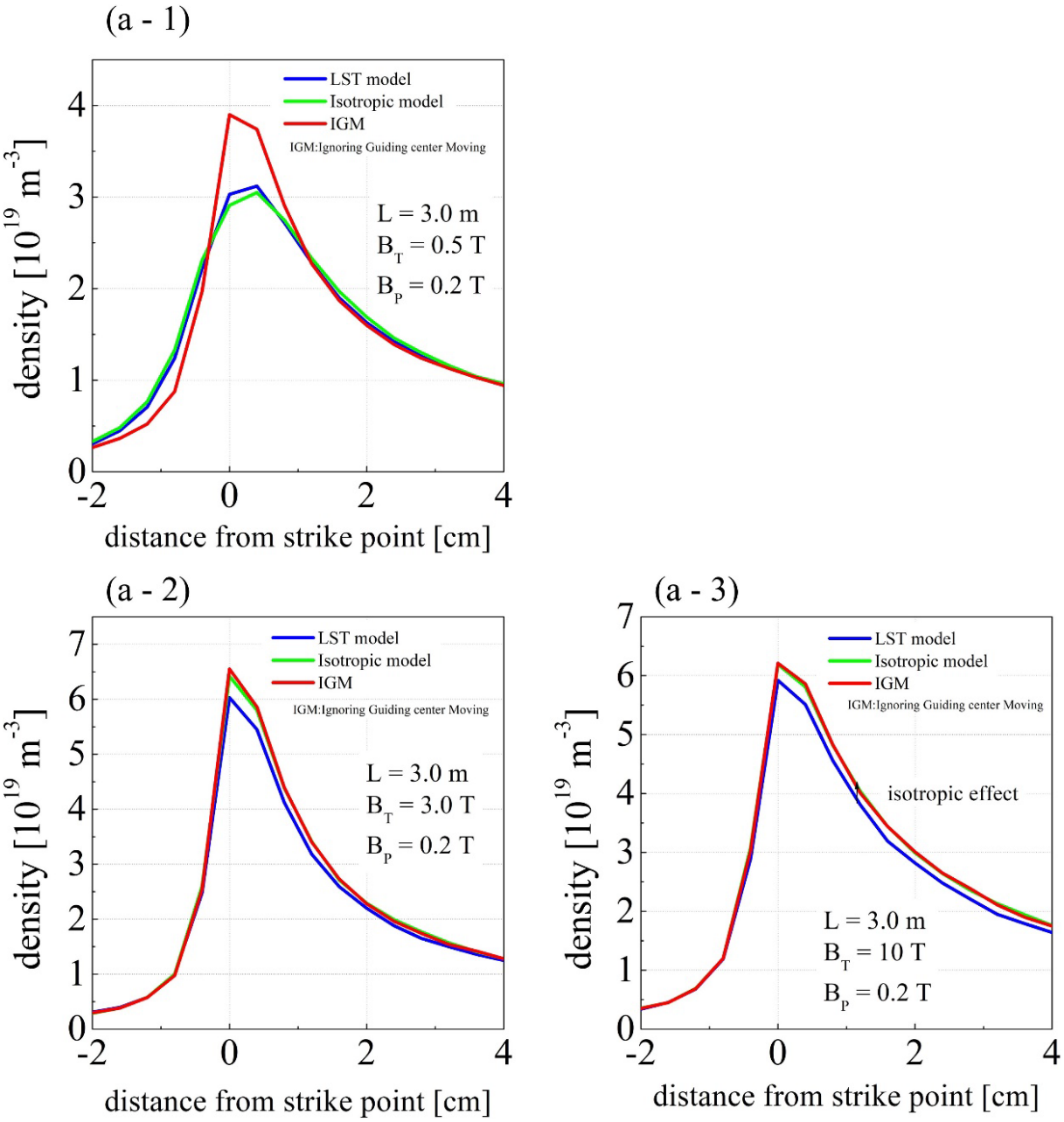

Fig. 7 Density profile at the divertor plate calculated via the LST, Isotropic and IGM models at (a-1) B_T = 0.5 T, (a-2) B_T = 3.0 T and (a-3) B_T = 10.0 T in the short leg divertor configuration.

and 3.3. By assuming the isotropic elastic scattering, obstruction effect of the elastic scattering might be overestimated, and details of it are discussed next section.

3.2 Effect of large-angle elastic scattering on the density profile at the divertor plate

The impact of LST on density profile at the divertor plate was also investigated. Density profiles at the divertor plate for the (a) short leg divertor and the (b) long leg divertor are illustrated in Figs. 7 and 8. Figures 7 and 8 (a-1, b-1), (a-2, b-2) and (a-3, b-3) display the results at B = 0.5, 3.0 and 10.0 T, respectively. Figures 7 and 8 display the density profiles calculated via the three models – LST, Isotropic, and IGM – represented by the blue, green and red lines, respectively. By comparing the density profile of the LST model (blue line) with that of the IGM model (red line), the effect of the elastic scattering on ion transport perpendicular to the magnetic field lines can be assessed. Furthermore, the distinction between the anisotropic scattering and the isotropic scattering can also be assessed by comparing the result of the LST model with the Isotropic model. For the short (long) leg divertor configuration, the peak density at the divertor plate calculated via the IGM model is 3.90, 6.55 and 6.21 (4.52, 10.3 and 14.0) $\times 10^{19}$ m^{-3} at B = 0.5, 3.0 and 10.0 T. The

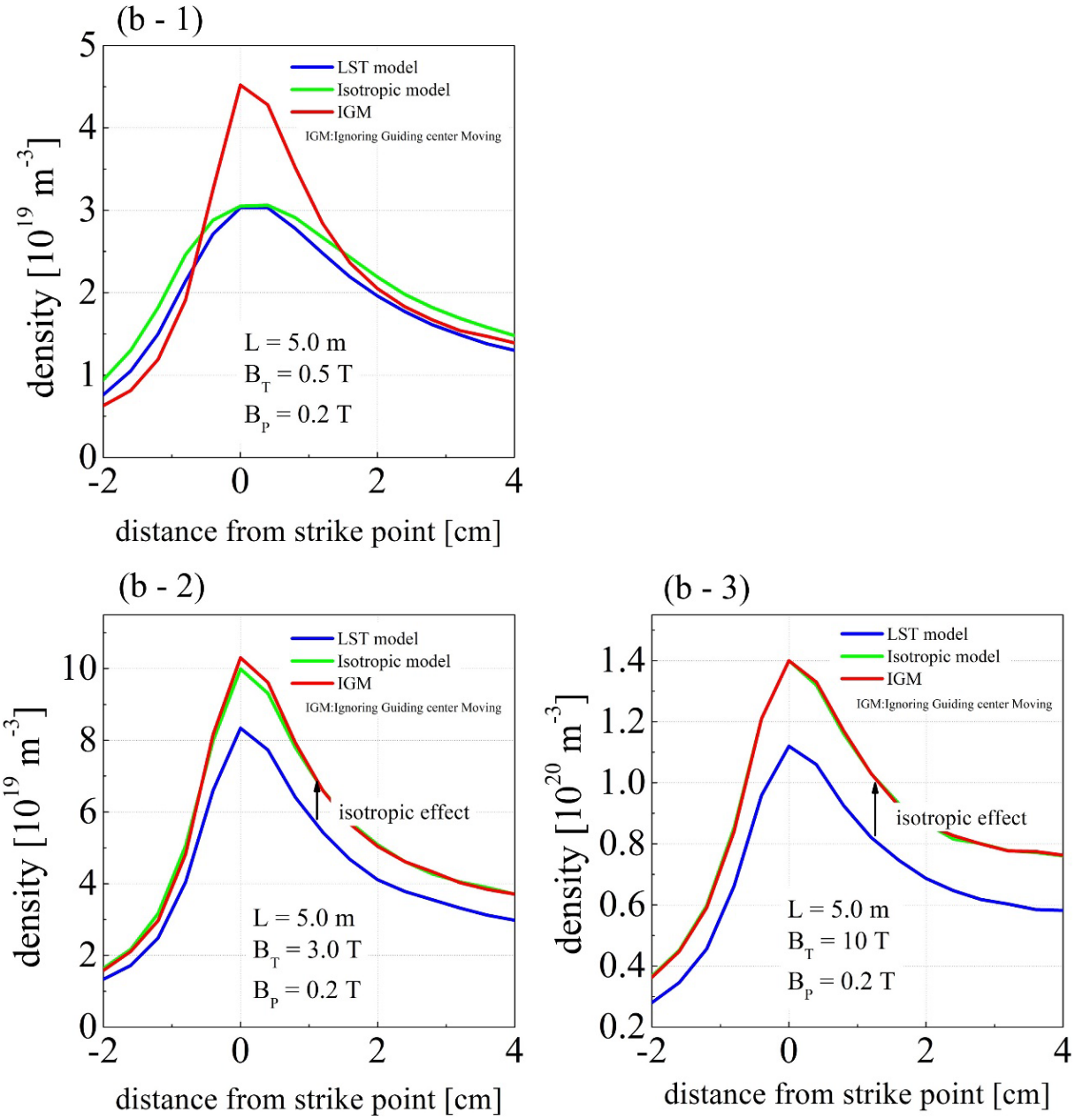

Fig. 8 Density profile at the divertor plate calculated via the LST, Isotropic and IGM models at (b-1) $B_T = 0.5$ T, (b-2) $B_T = 3.0$ T and (b-3) $B_T = 10.0$ T in the long leg divertor configuration.

peak density obtained using the LST model are 3.12, 6.03, and 5.92 (3.03, 8.34, and 11.2) $\times 10^{19}$ m^{-3} at $B_T = 0.5$, 3.0, and 10.0 T, respectively. Therefore, at low magnetic fields, the peak density is more reduced by the LST. At high magnetic fields, the effect of elastic scattering on ion transport perpendicular to the magnetic field is expected to be small because the Larmor radius is short. However, the density profiles calculated via the LST model in the strong magnetic field ($B_T = 10.0$ T) are almost identical and slightly smaller than those of the IGM model. Moreover, the decrease is unlikely to be due to the spreading of the ions. This is because the isotropic scattering assumption obstructs the flows of orbitally calculated ions toward the divertor plate excessively. The ions flow velocity toward the divertor plate was reduced by the isotropic elastic scattering and it took longer time for ions to reach the divertor plate than in the LST model. At $B_T = 10.0$, the time it takes for orbital ions generated at an average distance of 7.5 cm from the divertor plate to reach the divertor plate calculated via the LST (Isotropic) model was 0.196 (0.225) ms. Therefore, the assumption of isotropic scattering can lead to incorrect results. In this study, the background plasmas and neutrals are constant. Further study is needed to solve ions and neutrals with time evolution.

In order to assess pure effect of the large-angle elastic scattering on the ion transport, the density profiles at the di-

vertor plate for the short leg and long legs simulated via the LST model and anisotropic-IGM model were compared in Figs. 9 (a) and (b). The results of the LST (anisotropic-IGM) model are shown with solid (dotted) lines. The blue, black, and red lines represent the results at B_T = 0.5, 3.0, and 10.0 T, respectively. Since the LST and anisotropic-IGM models consider the differential cross section of the elastic scattering, the effect of neutral obstruction on ions flow velocity is equal in both models. In this comparison, the density profile at strong magnetic fields calculated via the LST model corresponded to the one obtained by the anisotropic-IGM model. At the weak magnetic fields, the density profile at the divertor plate was spread by the LST.

3.3 Dependence of the density peak and heat flux reduction ratio on magnetic field strength

The heat flux reduction ratio at the divertor plate was assessed at different magnetic fields. Figures 10 (a) and (b) show the dependence of the peak heat flux reduction ratio in the short leg and long leg derived from the LST (Isotropic) and IGM models on the magnetic field strength with black square (red point) symbols. The heat flux reduction ratio was calculated using Eq. (4).

The heat flux reduction ratio of the LST from the IGM model increases at $B_T \leq 3.0$ T and reaches approximately 16.8% (28.1%) at B_T = 0.5 T in the short (long) leg di-

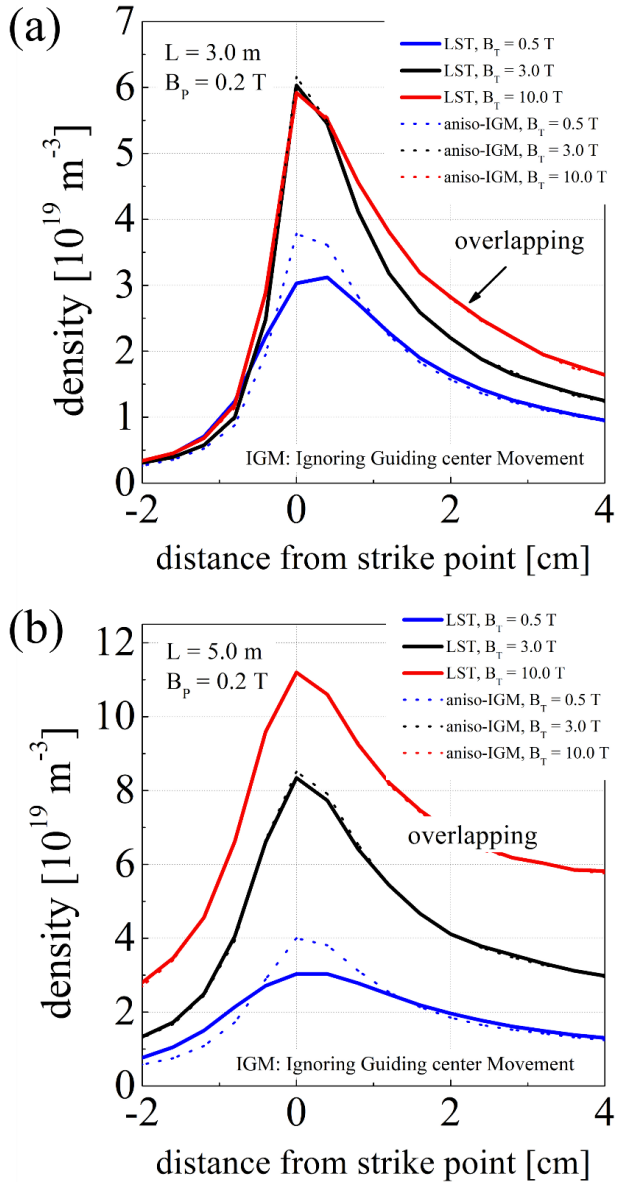

Fig. 9 Comparison of density profiles at the divertor plate calculated via the LST model and anisotropic-IGM models in the (a) short leg and (b) long leg divertor configurations.

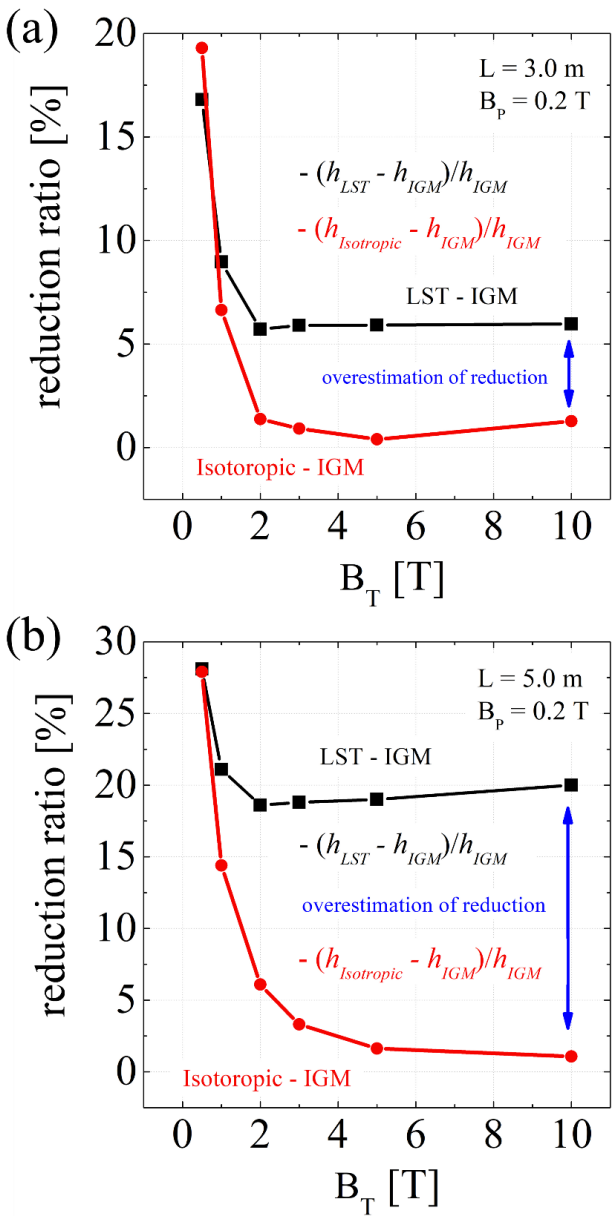

Fig. 10 Elastic scattering effect on the peak heat flux reduction ratio in the (a) short leg and (b) long leg divertor configurations.

vertor configuration. At $B_T \geq 5.0$, the peak heat flux reduction ratio of the LST model from the IGM model is approximately 6% (19%) in the short (long) leg divertor configuration. On the other hand, the reduction ratio of the Isotropic model from the IGM model approaches 0% in the strong magnetic field. As discussed in Sec. 3.2, the density profile calculated via the Isotropic model was larger than that of the LST model due to the excessive obstruction effect of the isotropic assumption on the ion flow. Since the peak densities calculated via the LST and IGM models do not correspond at the high magnetic fields, the peak heat flux reduction ratio of the LST model from the IGM model does not approach 0% at $B_T > 5.0$ T. In actual plasmas, as the ion density decreases, the ion temperature increases. However, in this study, since the background plasma is constant, the ion temperature calculated by orbital ions reflects the temperature of the background plasmas and does not increase.

In order to assess the impact of large-angle elastic scattering on the density profile and the heat flux reduction, the obstructive effect of the elastic scattering with neutral particles on the ion flow should be even, as between the LST and the anisotropic-IGM models. Figure 11 shows the peak heat flux reduction ratio of the LST model from the anisotropic-IGM model in the short (long) leg with the blue (black) line. In the high magnetic field, the reduction ratio approaches 0%. The LST is very limited when the magnetic field strength exceeds 10.0 T, because the Larmor radius and the distance travelled by the orbital particles in the radial direction are short. The reduction ratio increases at $B \leq 3.0$ T and reaches 15% (21%) in the short (long) leg divertor scheme. This reduction ratio is pure reduction effect of the large-angle elastic scattering transport on the heat flux. If the guiding center movement by the large-angle elastic scattering is ignored such as most of the integrated codes, the reduction effect of the large-angle elastic scattering on the heat flux is not considered.

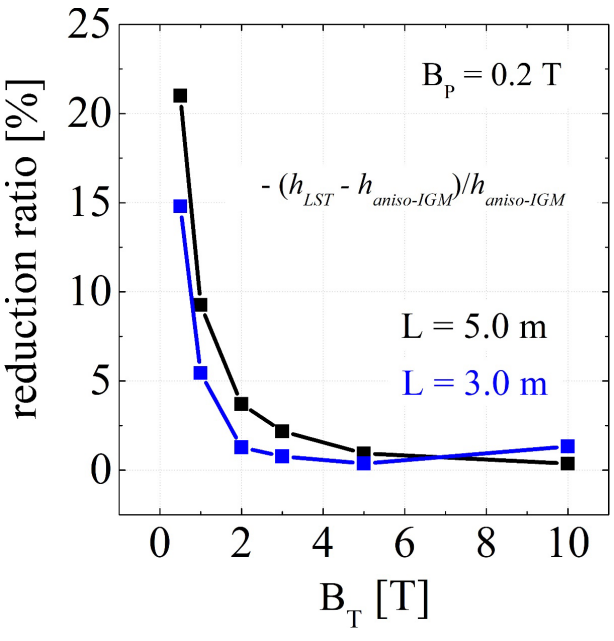

Fig. 11 Pure large-angle scattering effect on the peak heat flux reduction ratio in the short leg and long leg divertor configurations.

4. Conclusion

The effect of the large-angle elastic scattering between ions and neutral particles on ion transport, density profiles and heat flux were investigated by varying magnetic field strength for two divertor configurations, namely short and long leg divertors. We developed an orbit calculation code to adequately consider gyro-motion of ions around magnetic field lines and the effect of the large-angle elastic scattering on ion transport in a direction perpendicular to the magnetic field lines. The peak density and the heat flux were reduced due to the additional ion transport induced by the large-angle elastic scattering. In addition, the dependences of the density profile and the peak heat flux reduction ratio on the magnetic field strength were investigated. At low magnetic field strength, the large-angle elastic scattering effect on ion transport was enhanced. At $B_T = 0.5$ T, the peak heat flux was reduced by 17% (28%) compared to the IGM model in the short (long) leg divertor configuration due to the large-angle elastic scattering. The pure LST effect on the peak heat flux reduction was 15% (21%) in the short (long) leg divertor. In this work, we found that the peak heat flux is reduced due to a spread of the density profile induced by the large-angle elastic scattering transport. The assumption of isotropic elastic scattering may overestimate the obstruction effect of elastic scattering with neutral particles on ion flow velocity.

In this study, the background parameters for the orbit calculation were assumed to be constant. To confirm our findings regarding the large-angle elastic scattering effect, it will be necessary to study these phenomena using integrated codes in the future.

Acknowledgments

This work was supported by JST SPRING, Grant Number JPMJSP2136.

[1] K. Hoshino *et al.*, Fusion Eng. Des. **123**, 352 (2017).
[2] N. Asakura *et al.*, Nucl. Fusion **61**, 126057 (2021).
[3] N. Asakura *et al.*, Nucl. Mater. Energy **26**, 100864 (2021).
[4] P.M. Valanju *et al.*, Phys. Plasmas **16**, 056110 (2009).
[5] P.M. Valanju *et al.*, Fusion Eng. Des. **85**, 46 (2010).
[6] D.D. Ryutov, Phys. Plasmas **14**, 064502 (2007).
[7] D.D. Ryutov *et al.*, Phys. Plasmas **15**, 092501 (2008).
[8] A.S. Kukushkin *et al.*, Fusion Eng. Des. **86**, 2865 (2011).
[9] S. Wiesen *et al.*, J. Nucl. Mater. **463**, 480 (2015).
[10] X. Bonnin *et al.*, Plasma Fusion Res. **11**, 1403102 (2016).
[11] N. Asakura *et al.*, Fusion Sci. Technol. **63**, 75 (2013).
[12] N. Asakura *et al.*, J. Nucl. Mater. **463**, 1238 (2015).
[13] K. Hoshino *et al.*, Contrib. Plasma Phys. **52** (5-6), 550

(2012).
[14] H. Kawashima *et al.*, Plasma Fusion Res. **1**, 031 (2006).
[15] K. Shimizu *et al.*, Nucl. Fusion **49**, 3403070 (2009).
[16] P.S. Krstić and D.R. Schultz, At. Plasma-Mat. Interact. Data Fusion **8**, 1 (1998).
[17] D. Umezaki and H. Matsuura, Plasma Fusion Res. **16**, 2403021 (2021).
[18] D. Umezaki *et al.*, Contrib. Plasma Phys. e202300064 (2023).
[19] D. Tskhakaya and S. Kuhn, Contrib. Plasma Phys. **42** (2-4), 302 (2002).
[20] D. Tskhakaya and R. Schneider, J. Comp. Phys. **225**, 829 (2007).
[21] D. Tskhakaya *et al.*, Contrib. Plasma Phys. **47**, 563 (2007).
[22] T. Takizuka *et al.*, J. Nucl. Mater. **313**, 1331 (2003).
[23] T. Takizuka, Plasma Sci. Technol. **13**, 316 (2011).
[24] T. Takizuka, Plasma Phys. Cont. Fusion **59**, 034008 (2017).
[25] K. Shimizu, J. Nucl. Mater. **220**, 410 (1995).
[26] B.A. Trubnikov *et al.*, Rev. Plasma Phys. **1**, 105 (1965).
[27] K. Shimizu and T. Takizuka, J. Plasma Fusion Res. **71**, 1135 (1995).
[28] S.I. Braginskii, Trans. Processes Plasma Rev. Plasma Phys. **1**, 205 (1965).
[29] H. Matsuura and Y. Nakao, Phys. Plasmas **13**, 062507 (2006).
[30] H. Matsuura *et al.*, Plasma Fusion Res. **11**, 1403105 (2016).
[31] H. Matsuura *et al.*, IEEE Trans. Plasma Sci. **46**, 6 (2018).
[32] S. Sugiyama *et al.*, Phys. Plasmas **24**, 092517 (2017).
[33] S. Sugiyama *et al.*, Plasma Fusion Res. **14**, 3403123 (2019).
[34] S. Sugiyama *et al.*, Nucl. Fusion **60**, 076017 (2020).
[35] K. Kimura *et al.*, Rev. Sci. Instrum. **92**, 053524 (2021).
[36] K. Hoshino *et al.*, J. Nucl. Mater. **463**, 573 (2015).
[37] M.S. Islam *et al.*, Plasma Fusion Res. **16**, 2403049 (2021).
[38] R. Schneider *et al.*, Contrib. Plasma Phys. **46**, 1 (2006).
[39] P.C. Stangeby, Plasma Phys. Cont. Fusion. **43**, 223 (2000).
[40] T. Takizuka *et al.*, JAERI-Research 2003-010.
[41] K. Shimizu *et al.*, J. Nucl. Mater. **313-316**, 1277 (2003).
[42] M.H. Hughes and D.E. Post, J. Comp. Phys. **28**, 43 (1978).